Assessment of Molten Salt Pool Solidification with Decay Heat Using a 2D CFD-Informed 1D Steady-State Heat-Transfer Model

Jaemin Han^a, Ye Hwan Chun^a, Juhyeong Lee^a, JinHo Song^a, and Sung Joong Kim^{*a,b}
^aDepartment of Nuclear Engineering, Hanyang University, 222 Wangsimni-ro, Seongdong-gu, Seoul 04763,
Republic of Korea

^bInstitute of Nano Science and Technology, Hanyang University, 222 Wangsimni-ro, Seongdong-gu, Seoul 04763, Republic of Korea

*Corresponding author: sungjkim@hanyang.ac.kr

*Keywords: molten salt reactor, molten salt pool, natural convection, solidification, computational fluid dynamics

1. Introduction

The molten salt reactor (MSR), a concept from Generation IV nuclear technology, has garnered significant attention in recent years. In contrast to pressurized water reactors (PWRs), MSRs can operate at elevated temperatures (≥700 °C) and near atmospheric pressure [1]. The characteristics of MSRs facilitate the operation of a low-pressure vessel without the need for an additional pressurizer [2]. The use of low-pressure vessels reduces system volume per unit output, significantly contributing to miniaturization. Moreover, molten salt can eliminate the severe accidents considered in PWRs.

However, an accident, such as a reactor vessel failure, could lead to a large release of molten salt. In such an accident, the temperature of the released molten salt is critical because it governs fission-product release [3], which is conceptually analogous to the corium-coolability concern. In PWRs, severe accident management strategies have focused on in-vessel retention with external reactor-vessel cooling (IVR-ERVC) and on ex-vessel core catchers, both designed to ensure melt coolability [4].

For MSRs, natural cooling may be feasible even without these strategies, because the thermal-hydraulic behavior of a molten salt pool differs from that of a corium pool. MSRs operate at lower power than PWRs, the consequent decay heat is smaller, which lowers the Rayleigh number and consequently reduces the thermal load on vessels due to natural convection. This heat exchange with surrounding structures induces the formation of a crust and solidification, even without ERVC or core catchers. However, qualitative predictions are insufficient to demonstrate safety. Therefore, a quantitative assessment is necessary to predict the potential release of radioactive materials accurately.

In this study, the natural cooling and solidification potential of a molten salt pool is assessed, assuming an accident scenario involving a large release into the containment vessel. Initially, a two-dimensional (2D) computational fluid dynamics (CFD) analysis that includes decay heat determines the spatial distribution of boundary heat flux. These computed heat fluxes then serve as input to a one-dimensional (1D) steady-state heat-transfer model to assess crust formation and derive

the minimum cooling condition needed to ensure solidification. This approach provides the advantage of assessing coolability, including crust formation and its approximate thickness with fewer computational resources compared to an integrated CFD solidification model in Fluent.

2. Methodology

As the molten salt released into the containment vessel cools, a crust forms at the molten salt boundary. The interface between the molten salt and the crust was assumed to be at a constant temperature equal to the melting temperature of the salt, T_{melt} . Heat transfer to the boundary occurs due to the temperature difference between the bulk molten salt and T_{melt} . This process was simulated using 2D CFD to determine the boundary heat flux. This approach simplifies the cooling process of the molten salt pool with decay heat, thereby reducing the complexity of the analysis. The boundary heat flux of each cell calculated by 2D CFD was then used as a boundary condition for a 1D model to determine the crust thickness and minimum cooling conditions.

2.1. Geometry and boundary conditions

Figure 1 shows the computational domain and boundary conditions. The model assumes a 2D axisymmetric geometry with the x-axis as the axis of symmetry. A constant temperature boundary condition, $T_{\rm melt}$, was applied to the entire molten salt pool boundary. Two decay heat conditions, 3 MW and 0.5 MW, were selected based on a decay heat curve for a one-year operational history. The decay heat was applied as a uniform volumetric heat source throughout the entire volume of the molten salt pool.

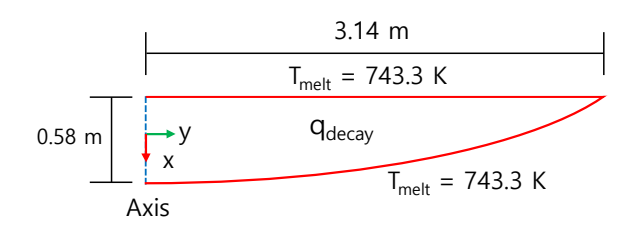


Fig. 1. Computational domain and boundary conditions.

Table 1 presents the thermophysical properties of NaCl-KCl-UCl₃, which were used as input to the CFD simulation. A structured mesh was generated using ANSYS Meshing. The mesh was constructed to maintain a maximum $y^+ \le 5$ for the 3 MW case.

Figure 2 shows the results of the mesh independence test conducted under the 3 MW condition. The temperature profiles along the depth at points B and C were compared. For the 82,000 and 102,000-cell meshes, the maximum deviation from the reference mesh (123,200 cells) was less than 1%. Considering computational resources, the 82,000-cell mesh was used for the main analysis.

Table 2 summarizes the analysis conditions. The commercial CFD code ANSYS Fluent 2024 R1 was used, and the SST k- ω model was used to simulate the turbulent flow arising from natural convection. A time step of 1 s was used, and the total simulation time ranged from 8,000 to 32,000 seconds, depending on the decay heat condition. The heat flux at the top and bottom boundaries was calculated by averaging the data over the final 1,000 seconds after reaching a quasi-steady state.

Table I: Thermodynamic properties of NaCl-KCl-UCl₃ for CFD

Properties	Values	
ρ [kg/m³]	3476 ~ 2875	
C _p [J/kg·K]	609.5 ~ 547.5	
k [W/m·K]	0.407 ~ 0.319	
μ [kg/m·s]	0.005015 ~ 0.001257	
T _{melt} [K]	743.3	

Table II: Numerical analysis condition

Tueste 11: 1 (uniterious unus) sis contaition				
Parameters		Values		
Viscous model		SST k-ω		
Spatial	Gradient	Least squares cell- based		
discretization	Pressure	Body Force Weighted		
scheme	Momentum	2 nd order upwind		
	Energy	1st order upwind		
Time step		1 s		
Overall simulation time		8,000 ~ 32,000 s		
Averaging	Interval	1,000 s		

2.2. Analytic 1D model for crust thickness

The heat fluxes at each boundary cell obtained from the CFD were directly used as input values in the 1D steady-state heat-transfer model to evaluate the local crust thickness. As a result, the crust thickness at each position is estimated by this methodology. Figure 3 shows the heat transfer path from the molten salt pool boundary, through the crust and the containment vessel, to the ambient, which was modeled as a 1D steady-state thermal resistance network. The heat flux from the CFD

is transferred via conduction through the crust and the containment wall, and then via convection and radiation to the ambient.

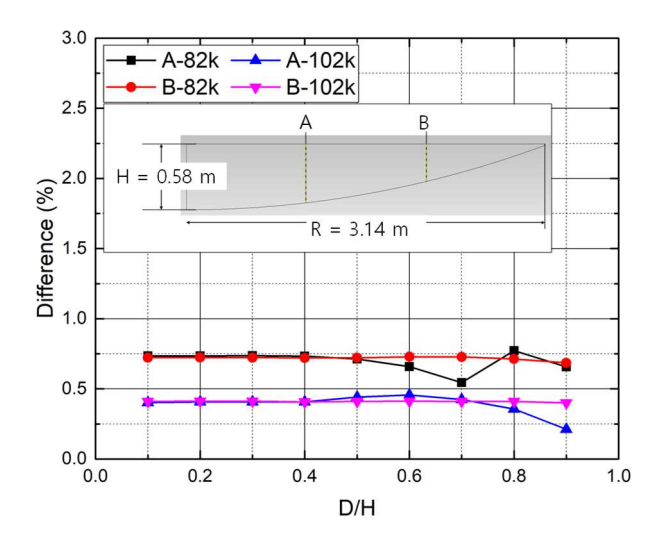


Fig. 2. Result of mesh independence test at 3 MW.

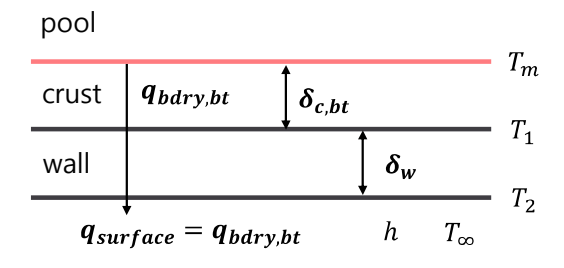


Fig. 3. Schematic of heat transfer at the bottom.

The energy balance equation is expressed as Eq. (1) when considering only convection, and as Eq. (2) when considering both convection and radiation. Here, kc and kw are the thermal conductivities of the crust and the containment vessel, respectively, and $\delta_{c,b}$ and δ_w are their thicknesses.

$$q_{bdry,bt} = k_c \frac{T_m - T_1}{\delta_{c,bt}} = k_w \frac{T_1 - T_2}{\delta_w} = h(T_2 - T_\infty) (1)$$

= $h(T_2 - T_\infty) + \varepsilon \sigma (T_2^4 - T_\infty^4)$ (2)

From Eq. (1), the critical heat transfer coefficient, h_{crit} , is defined as the minimum value of the heat transfer coefficient required for crust formation to begin, that is, the moment $T_m \ge T$ is satisfied, and is given by Eq. (3).

$$h_{crit} = \frac{q_{bdry,bt}}{T_m - T_{\infty} - q_{bdry,bt} \frac{\delta_w}{k_w}}$$
(3)

Figure 4 shows a schematic of heat transfer at the top of the molten salt pool. In the figure, "solid" represents a virtual structure above the molten salt pool. Assuming a steady-state where all the heat flux, $q_{bdrytop}$, is transferred

to this structure via radiation, the relationship is given by Eq. (4). From this, the critical top structure temperature, $T_{crit,solid}$, is defined as the maximum temperature of the structure that allows for crust formation and is given by Eq. (5).

$$q_{bdry,top} = k_c \frac{T_m - T_{top}}{\delta_{c,top}} = \varepsilon \sigma \left(T_{top}^4 - T_{solid}^4\right) \quad (4)$$

$$T_{crit,solid} = \left(T_m^4 - \frac{q_{bdry,top}}{\varepsilon\sigma}\right)^{\frac{1}{4}} \tag{5}$$

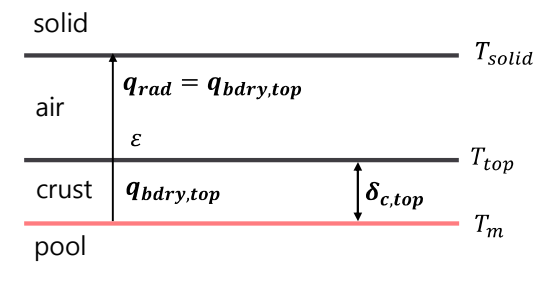


Fig. 4. Schematic of heat transfer at the top.

Table 3 lists the main parameters used in the 1D model calculations. The thermal conductivity of the crust, k_c , reflects the properties of NaCl-KCl-UCl₃, while k_w reflects that of SS316. The heat transfer coefficient was varied to compare natural convection in air (10 W/m²·K) with a stronger convection (20 W/m²·K).

Table III: Assume values for 1D model

Paramters	Values	
$T_{\infty}[K, {}^{\circ}\!C]$	328.15, 55	
$k_c [W/m \cdot K]$	0.4	
$k_w [W/m \cdot K]$	20	
$h [W/m^2 \cdot K]$	10	
	20	
$\delta_{\rm w}$ [mm]	10	
	100	
$\sigma [W/m^2 \cdot K^4]$	5.67×10 ⁻⁸	
T_{solid} [K, °C]	328.15, 55	
ε (emissivity)	1	
	0.5	

3. Results and discussion

3.1. Heat flux

The results showed opposing heat flux distribution patterns at the top and bottom boundaries. Figure 5 compares the heat flux distributions at these boundaries according to the nondimensional distance from the center (r/R) for each decay heat condition. At the top boundary, for both the 3 MW and 0.5 MW conditions, the heat flux decreased with increasing distance from the center of the pools. Conversely, the heat flux at the bottom boundary tended to increase with distance from the center. As

shown in Figure 6, this contrasting phenomenon is primarily driven by a natural convection: the relatively hot molten salt rises to the center of the top boundary (1), flows toward the edge (2), and subsequently descends along the sloped bottom boundary (3), (4).

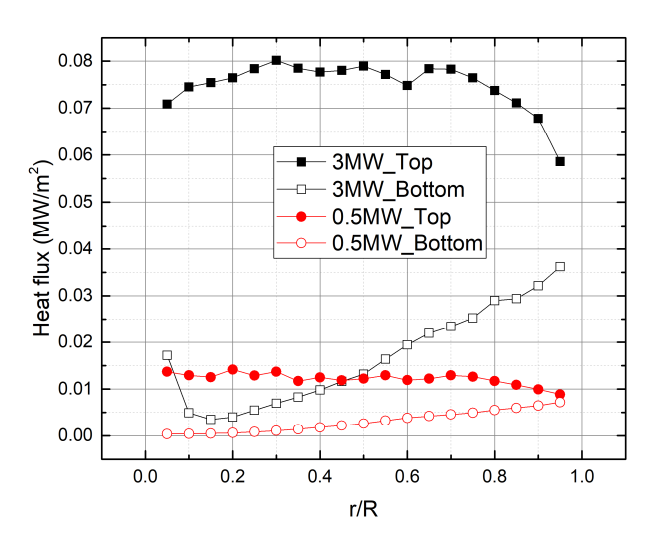


Fig. 5. Comparison of heat flux at top and bottom boundaries by decay heat.

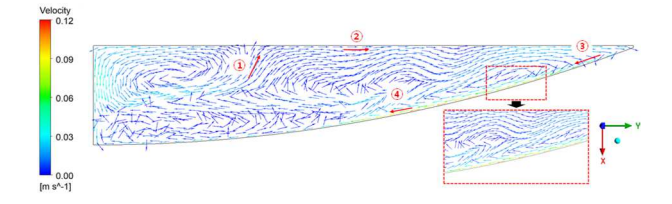


Fig. 6. Velocity vectors for the 3 MW condition.

3.2. Crust thickness

The analysis of the top crust thickness, based on Eq. (4), showed that for the 3 MW condition, no crust was formed by radiation cooling alone. For the 0.5 MW condition, a crust formed, but it thinned toward the center. For the bottom crust, calculated using Eq. (1) and Eq. (2), the results indicated that even when considering radiation, no crust formed at specific locations under the 3 MW condition. Because of the opposing heat flux patterns, the crust thickness distribution also showed an inverse relationship: the top crust grew thicker further from the center, while the bottom crust grew thinner.

3.3. Required cooling conditions

The difference in heat flux distribution between the boundaries implies that the required cooling performance varies for each boundary. Therefore, to provide a metric for design, the minimum cooling conditions necessary for crust formation at each boundary were quantified.

For the top boundary, the critical solid temperature, $T_{\text{crit,solid}}$, was calculated using Eq. (5). Under the 3 MW condition, $T_{\text{crit,solid}}$ was undefined at all locations,

indicating that the crust formation condition could not be satisfied by radiation cooling alone. For the 0.5 MW condition, $T_{\text{crit,solid}}$ was lowest at the center, corresponding to the region of highest heat flux. However, when the emissivity was reduced from 1.0 to 0.5, $T_{\text{crit,solid}}$ became undefined at most locations.

For the bottom boundary, the critical heat transfer coefficient, h_{crit} , was calculated using Eq. (3). For the 3 MW condition with $T_{\infty}=328.15$ K, the maximum value of h_{crit} varied with the containment wall thickness (δ_w) . For instance, the maximum h_{crit} was calculated to be approximately 769 W/m²·K for $\delta_w=100$ mm, and 172 W/m²·K for $\delta_w=10$ mm. In contrast, for the 0.5 MW condition, the maximum h_{crit} was on the order of tens of W/m²·K, confirming that heat removal was feasible even with a relatively low cooling performance.

3.4. Discussion

These quantitative requirements are consistent with the parameter contrasts summarized in Table 4. Compared with a PWR corium pool, the MSR molten salt pool exhibits substantially lower volumetric heat generation, and a correspondingly lower Rayleigh number. These differences imply weaker natural convection intensity and smaller boundary heat fluxes in a molten salt pool than in a corium pool. This explains why heat removal is feasible with a relatively lower cooling performance compared to strategies such as IVR-ERVC. Therefore, it is reasonable that the required cooling performance calculated in Section 3.3 is lower than that for a PWR corium pool.

Table IV: Qualitatively compares representative molten-pool parameters for PWR corium and MSR molten salt. The MSR values correspond to the assumptions adopted in this study.

Parameters	PWR Corium pool [5]	MSR Molten salt pool
Bulk temperature [K]	High (~3000)	Low (~923)
Volumetric heat generation [MW/m³]	High (~2.9)	Low (~0.33)
Rayleigh number	High (~10 ¹⁶)	Low (~10 ¹³)
Boundary heat flux at top [MW/m²]	High (~1.6)	Low (~0.08)

4. Conclusion

In this study, the natural cooling and solidification potential of a molten salt pool under a large release scenario was quantitatively evaluated. The boundary heat flux distribution was first analyzed using a 2D CFD analysis. This data was then used as an input to a 1D steady-state heat-transfer model to derive the required cooling conditions for the top and bottom boundaries. The main conclusions are as follows:

 For the top boundary, solidification is not feasible with radiation cooling alone under the 3 MW condition. Even for the 0.5 MW condition, cooling by radiation alone is insufficient when the

- emissivity is low ($\varepsilon = 0.5$). Therefore, additional heat transfer modes beyond radiation are required for stable solidification of the top boundary.
- 2. At the bottom boundary, the thermal load is concentrated at the outer edge and increases with distance from the center. For the 3 MW condition, the natural air convection condition (10, 20 W/m²·K) is insufficient for solidification. A design with enhanced cooling performance, such as free or forced convection with a liquid coolant, or an increased heat transfer area using fins, is required. In contrast, for the 0.5 MW condition, heat removal is feasible with a heat transfer coefficient on the order of tens of W/m²·K.

Future work aims to perform a more comprehensive analysis that includes more realistic boundary conditions by modeling conjugate heat transfer, and a solidification and melting model to simulate transient phenomena such as crust formation and remelting.

ACKNOWLEDGMENTS

This work was supported by the National Research Foundation of Korea(NRF) grant funded by the Korea government(MSIT) (RS-2025-02310831), and the Human Resources Development of the Korea Institute of Energy Technology Evaluation and Planning (KETEP) grant funded by the Korea government Ministry of Knowledge Economy (RS-2024-00439210).

REFERENCES

- [1] J. Serp, M. Allibert, O. Beneš, S. Delpech, O. Feynberg, V. Ghetta, D. Heuer, D. Holcomb, V. Ignatiev, J. L. Kloosterman, L. Luzzi, E. Merle-Lucotte, J. Uhlíř, R. Yoshioka, and D. Zhimin, The Molten Salt Reactor (MSR) in Generation IV: Overview and Perspectives, Progress in Nuclear Energy, Vol. 77, pp. 308-319, 2014.
- [2] D. LeBlanc, Molten Salt Reactors: A New Beginning for an Old Idea, Nuclear Engineering and Design, Vol. 240, No. 6, pp. 1644-1656, 2010.
- [3] S. Nichenko, J. Kalilainen, and T. Lind, MSR Simulation with cGEMS: Fission Product Release and Aerosol Formation, Journal of Nuclear Engineering, Vol. 3, No. 1, pp. 105–116, 2022.
- [4] W. Ma, Y. Yuan, and B. R. Sehgal, In-vessel Melt Retention of Pressurized Water Reactors: Historical Review and Future Research Needs, Engineering, Vol. 2, No. 1, pp. 103–111, 2016.
- [5] F. B. Cheung, et al., In-vessel Retention Strategy for High Power Reactors: K-INERI Final Report, Idaho National Laboratory, INEEL/EXT-04-02561, 2005.